Characteristics of a modified H13 hot-work tool steel fabricated by means of laser beam powder bed fusion

Downloaded from: https://research.chalmers.se, 2024-03-20 11:15 UTC

Citation for the original published paper (version of record):

Yuan, M., Cao, Y., Karamchedu, S. et al (2022). Characteristics of a modified H13 hot-work tool steel fabricated by means of laser beam powder
bed fusion. Materials Science & Engineering A: Structural Materials: Properties, Microstructure and Processing, 831. http://dx.doi.org/10.1016/j.msea.2021.142322

N.B. When citing this work, cite the original published paper.

research.chalmers.se offers the possibility of retrieving research publications produced at Chalmers University of Technology.
It covers all kind of research output: articles, dissertations, conference papers, reports etc. since 2004.
research.chalmers.se is administrated and maintained by Chalmers Library

(article starts on next page)

Materials Science & Engineering A 831 (2022) 142322

Contents lists available at ScienceDirect

Materials Science & Engineering A

journal homepage: www.elsevier.com/locate/msea

Characteristics of a modified H13 hot-work tool steel fabricated by means of laser beam powder bed fusion

Miwen Yuan [a,b], Yu Cao [a,*], Seshendra Karamchedu [c], Seyed Hosseini [a,d], Yiming Yao [a], Johan Berglund [a,d], Libin Liu [b], Lars Nyborg [a]

[a] Department of Industrial and Materials Science, Chalmers University of Technology, Gothenburg, 41296, Sweden
[b] School of Materials Science and Engineering, Central South University, Changsha, 410083, PR China
[c] Uddeholms AB, Hagfors, 63885, Sweden
[d] RISE Research Institutes of Sweden AB, Argongatan 30, 431 53, Mölndal, Sweden

ARTICLE INFO

Keywords:
Softening resistance
Tool steel
Additive manufacturing
Mechanical properties
Heat treatment

ABSTRACT

In the present study, a modified H13 hot-work tool steel (M-H13) was fabricated by laser beam powder bed fusion (LB-PBF). The effect of two types of post processing, direct tempering from as-built condition (DT) and conventional quenching followed by tempering (QT), on the microstructure and mechanical properties was evaluated. The typical microstructure in QT condition was tempered martensite with carbides along lath boundaries. In DT condition, melt pool boundaries and cellular structure from as-built condition were still observed. While comparable tensile properties and hardness were obtained, DT samples exhibited significantly lower impact toughness compared to QT samples. This was attributed to the difference in work hardening ability and strain rate sensitivity originating from different microstructures obtained under these two heat treatment conditions. The study was also focused on the softening behavior and the correlation with the microstructure of the two post treatments at the elevated temperatures. It was found that the DT samples showed lower thermal softening compared to QT samples. The evolution of carbides was discussed based on the microanalysis results and the JMatPro simulation.

1. Introduction

Additive Manufacturing (AM) provides the advantage of reducing the lead time of production, producing net-shape parts and creating components with complex features. These characteristics make it attractive for industrial applications [1]. Laser beam Powder-Bed-Fusion (LB-PBF), which is sometimes referred to as Selective Laser Melting (SLM) is one of the most prominent AM techniques in the context of metallic materials. Various alloys (Nickel-, ferritic-, Titanium-, Aluminum-base) processed by LB-PBF have hence been studied in terms of their mechanical properties, processibility, microstructures etc. [2–5]. The produced components usually presented a unique microstructure with evident solidification tracks and fine cellular dendritic structure, which is hypothesized to be responsible for high mechanical properties [6,7]. High cooling rate varying from a magnitude of 10^3–10^8 K/s is a major feature of LB-PBF [8]. Important factors that influence cooling rate are input energy density, preheating temperature, and thermal conductivity. Theoretically, adjusting these parameters could tailor the microstructure of components manufactured by LB-PBF.

Hot work tool steel H13 having high strength with reasonable ductility, good hardenability and thermal softening resistance is one of the widely used steels in hot stamping tools [9]. In the recent years, there were a number of studies on this high strength steel produced by LB-PBF [10–13]. Mertens et al. [10] showed compressive residual stress was found in the printed layers of H13 tool steel manufactured by LB-PBF due to volume expansion caused by martensitic phase transformation. Preheating the building plate to 400 °C was shown to change the residual stress to tensile state gradually. Regarding the tensile properties, the yield strength and total elongation could reach 1073 ± 72 MPa and 4% respectively in the LB-PBF H13 steel printed with preheating at 400 °C. However, it is still lower than that of the conventionally produced and wrought (1010 °C/oil quench + 605 °C tempering) parts which exhibit a yield strength of 1290 MPa with 15% elongation [14]. Wang et al. [11] reported the orientation dependence of mechanical properties in the LB-PBF produced H13. Higher yield strength was observed along the building direction (1564 MPa)

* Corresponding author.
E-mail address: yu.cao@chalmers.se (Y. Cao).

https://doi.org/10.1016/j.msea.2021.142322
Received 7 June 2021; Received in revised form 8 November 2021; Accepted 9 November 2021
Available online 12 November 2021
This is an open access article under the CC BY-NC-ND license (http://creativecommons.org/licenses/by-nc-nd/4.0/).

compared to the horizontal one (1288 MPa). Although yield strength reported was comparable to the wrought H13, the elongation at break (5–6%) was still lower. Optimizing scan strategy may improve the yield strength and tensile strength to 1342 ± 76 MPa and 1704 ± 30 MPa respectively [12], which are comparable to the conventional H13 [14]. However, the elongation decreased dramatically to 1.55 ± 0.05%, which is significantly lower than that of conventional counterparts. In the published literature [10–12], most of the H13 steels fabricated by LB-PBF are still inferior to the conventional H13 steels in terms of tensile properties. A slight modification of composition of the H13 grade could be a possible way to overcome these drawbacks. Improving printability could effectively decrease the defects in AM steel, which could be a way to improve the mechanical properties [15]. In the present research, a new steel with a modified composition based on the standard H13 steel is studied. Lower C content in this steel is expected to optimize the printability. Additionally, adjusting other alloy elements (adding W, decreasing the content of Cr, V and increasing the content Mo) aims to improve the steel's softening resistance at high temperatures.

It is well known that existence of porosity, high level of thermal stress and cracking susceptibility make the production of a high-quality parts by LB-PBF difficult [16]. In spite of some improvements in the AM-part quality by optimizing the processing parameters [3,12,17–19], most of the as-printed components cannot meet the demands of industrial applications. Post heat treatments are often necessary in order to remove the residual stress and maintain the part-geometry [19,20]. Yoo et al. [21] demonstrate that the yield strength of LB-PBF produced 17-4 PH stainless steel can be improved from 620 MPa to 1100 MPa through a proper post treatment. Chen et al. [22] also investigated the effect of heat treatment on the mechanical properties of LB-PBF produced 5CrNi4Mo tool steel. The results show that the heat treatment (640 °C/3 h) can not only enhance the tensile strength, but also improve the elongation and the fracture toughness. Stress relieving and recrystallization play a vital role in these changes. In the post treatments of AM products, the austenitization or solution treatment is less involved because the fine cellular microstructure obtained from the AM process is not retained after such treatments. So far, most of the published work concerning H13 steel produced by LB-PBF focused on the mechanical properties. Only a few investigations focus on evaluating the thermal softening or the so-called temper-back resistance [23]. Considering that hot working tool steel is exposed to high temperature during service, softening resistance at elevated temperatures is of great importance.

In this study, a modified H13 (M-H13) steel produced through LB-PBF is dealt with. The main focus is on understanding the effect of post treatment on the microstructure and mechanical behavior, especially the tensile and impact toughness properties. Due to the rapid cooling experienced by the material during the LB-PBF process, an intrinsic "quenching" is already realized. Based on this, a direct tempering was performed on as-built samples. In comparison, a traditional post heat-treatment including austenitization and tempering was also used on as-built parts. For hot-work applications, the resistance of the steel to softening at high temperatures is critical and determines the life of the tools. It was hence evaluated by means of hardness measurements and microstructural observation after long term exposure at elevated temperatures. Furthermore, to aid phase identification, JMatPro simulation was also performed.

2. Experimental

2.1. Materials and sample preparation

The nominal composition of the investigated steel is X33CrMoNiW3–2. It was based on conventional H13 (X40CrMoV5-1) with small modification to optimize the properties at elevated temperatures for the intended applications. Lower C content in this steel is expected to optimize the printability. Additionally, adjusting other alloy elements (adding W, decreasing the content of Cr, V and increasing the content Mo) aims to improve the steel's softening resistance at high temperatures. The alloy powder was provided by Uddeholms AB (Sweden). All specimens were produced by a SLM 125 HL system (SLM solutions Group AG), equipped with a single 400 W YAG-fiber laser with a wavelength of 1070 nm. The equipment had a build area of 125 × 125 mm^2. During the printing process, argon of a 4.6 purity (Linde Group) was used as a protective atmosphere to prevent oxidation. Table 1 shows the process parameters used for the manufacturing of the specimens, which are the standard parameters for H13 provided by SLM Solutions. The baseplate was preheated at 200 °C to avoid cracking and distortion during manufacturing. All specimens were manufactured using a contour-core strategy in which the core was melted in a bi-directional stripe pattern. After printing, the relative density of the fabricated samples measured by ImageJ software is 99.94%. ± 0.1, which is comparable to that of standard H13 samples (99.92% ± 0.08).

After printing, the samples were subjected to two different post processing conditions. a) The builds were quenched and tempered (QT) in a traditional heat treatment process used in the case of hot work tool steel. In this route, the samples were heated to 1020 °C for 30 min followed by quenching in oil. Subsequently, the samples were tempered twice at 580 °C for 2 h. b) Considering the possible martensite formation due to high cooling rate involved in the LB-PBF process, in the second route, the parts were directly tempered (DT) at 625 °C for 2 h twice (2 x 2h), to simplify the process. Another purpose this treatment serves is internal stress relief and reducing retained austenite content [24]. To examine the softening behavior (temper back resistance) at high temperatures, the samples with the two different post treatment conditions were exposed to isothermal holding at 550 °C and 600 °C for 5 h, 25 h, 50 h and 100 h, respectively. Fig. 1 summaries the post processing and softening treatments performed on the builds.

2.2. Microstructure observation

After printing and post treatment, sample cubes were prepared for metallographic examination using SiC abrasive paper followed by polishing using diamond suspension until mirror finish was achieved. In order to reveal the microstructure, chemical etching was performed using an etchant containing 10 g picric acid in 100 ml ethanol at room temperature. The phase constituents were analyzed by XRD using a Bruker D8 Advance equipped with Cr anode ($\lambda_{K\alpha1}$ = 2.29 Å) at an acceleration voltage of 35 kV. The diffraction angle 2θ range was 30° < 2θ < 155° and the step-size was 0.05° with 10 s analysis time per step. The diffraction patterns were evaluated using Bruker Diffrac.Suite Eva 4.x with PDF-4+ 2019 diffraction database. The microstructure changes were observed under an optical microscope (OM) and a Zeiss LEO Gemini 1550 field emission gun scanning electron microscope (FEG-SEM). Phase identifications were performed with the assistance of scanning transmission electron microscopy (STEM) and transmission electron microscopes (TEM). The thin-foil samples for STEM and TEM were prepared by grinding them to a thickness of 100 μm and electrolytic polishing using the Struers A2 electrolyte at 2 °C. FEI Tecnai T20 TEM was operated at 200 KV during the examination. The SEM-STEM HAADF Imaging and EDS analysis on the TEM sample were performed at a Zeiss Gemini 450 FEGSEM equipped with an Oxford ULTIM Max100 detector operated at 30 kV. Furthermore, JMatPro software (version of 11.2) was used as a complement for microstructure analysis.

2.3. Mechanical tests

Charpy V-notch impact testing was performed on a Roell Amsler RKP instrument. The specimens used for the testing were machined to the dimensions of 55 × 10 × 10 mm^3. The 45° V-shape notch of the specimens had a tip radius of 0.25 mm and a depth of 2 mm. The pendulum was preset to 150 J. Vickers Hardness was measured on the polished surface of cubes with different treatment using Struers DuraScan-70 G5, under a load of 10 Kg with a dwell time of 15 s. Six indentations were

Table 1
Processing parameters applied in manufacturing of M-H13 by LB-PBF.

Laser power (W)	Scan speed (mm/s)	Layer thickness (μm)	Hatch distance (μm)	Spot size (μm)	Preheating (°C)	Atmosphere	Pressure (mbar)
175	720	30	120	65	200	Argon	12

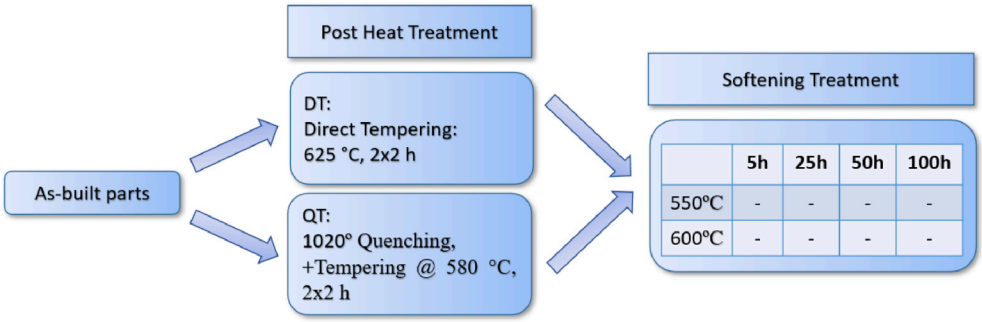

Fig. 1. Post processing and softening treatment performed on the builds.

made to obtain the average hardness. The tensile tests were performed using Instron 4505 at strain rate of 10^{-4} and 10^{-1} s^{-1}. The gauge length of the extensometer was 12.5 mm. The round tensile bars have a gauge length of 25 mm and a diameter of 5 mm. After testing, the fracture surfaces were examined by means of SEM.

3. Results

3.1. Influence of post-treatment

3.1.1. Microstructure

Fig. 2 shows the optical microscopy images of as-built, DT and QT samples from X-Z, Y-Z and X–Y planes respectively, with the building direction parallel to the Z-direction. Distinct melt pool boundaries were observed in the as-printed material (Fig. 2a). On the X–Y plane, the scan tracks along two directions were observed. This scanning strategy could effectively prohibit the epitaxial growth during the building process. Kono et al. [25] pointed out that epitaxial growth occurs when the heat flow direction is coincident with certain crystallographic orientation of the substrate material. From the observation in the present study, no distinct epitaxial growth was found due to the scanning strategy applied. Occasionally, some elongated melt pools were observed in X-Z plane in Fig. 2a. After the DT process, the boundaries still exist, but are less distinct compared to those in the as-printed condition (Fig. 2b). The QT

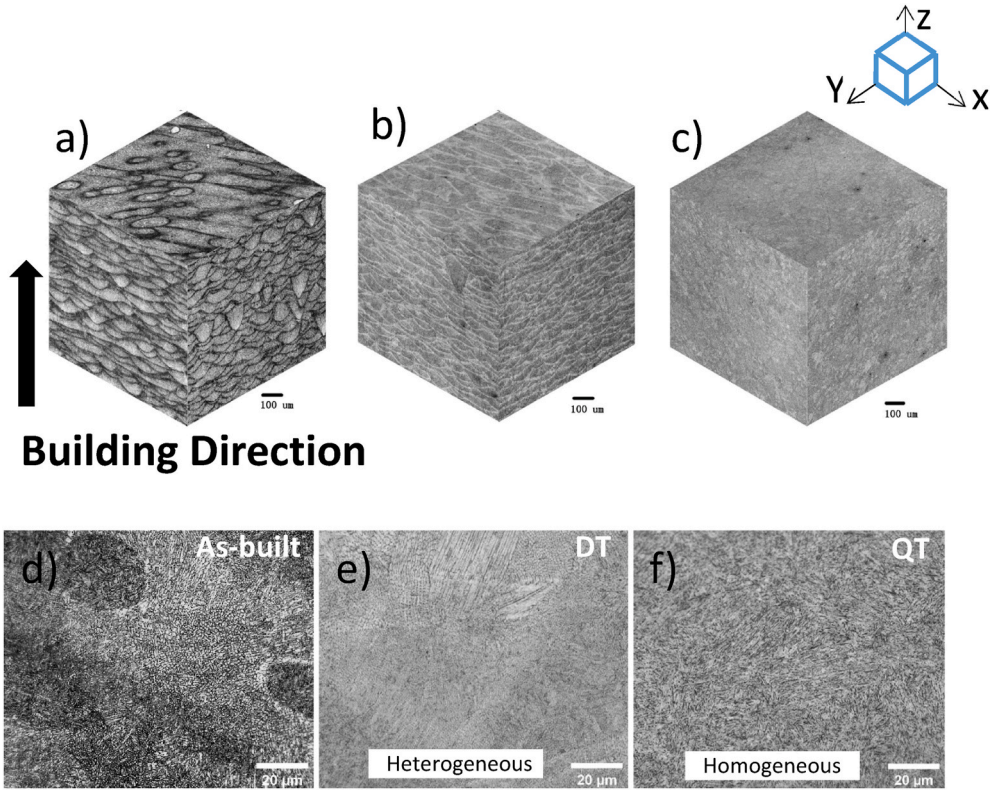

Fig. 2. Optical microscopic images of (a) as-built, (b) DT, (c) QT states in the XZ, YZ and XY planes; (d), (e) and (f) are the OM images with higher magnification from XY planes of as-built, DT and QT states samples.

process results in the disappearance of these melt pool boundaries (Fig. 2c), and the microstructure becomes more homogeneous because of the high temperature austenitization. At higher magnifications, the microstructure of QT sample is distinctly more homogeneous than that in the as-built and DT samples (Fig. 2d, e and f).

Fig. 3 shows the SEM images of DT and QT samples at different magnifications. In DT samples, cellular structure from as-built condition was maintained. The cellular structure on the sectioned surface presents different morphology corresponding to varied grain orientations (Fig. 3a). Theoretically, there should be a large number of carbides at the cell boundaries. However, the small size of carbides and the limited resolution of SEM make the observation of carbides difficult. The size of the cellular features was about 0.7 μm, as indicated in Fig. 3b. It is a consequence of the high cooling rate (typically about 10^5 K/s) [26] in LB-PBF process. Similar solidification structure has been found to be beneficial to the high strength in many alloys fabricated by LB-PBF, such as X40CrMoV5-1 tool steel, AlSi10Mg and Inconel 718 [4,5,27]. In QT samples, austenitization led to homogenization by diffusion at high temperature, the cellular structure disappeared completely after the quenching and double tempering treatment. Only tempered lath martensite was observed, which constituted very fine structure with a lath width of ~0.7 μm, as shown in Fig. 3c and d. Furthermore, rod like shaped precipitates were observed along the lath structure, as indicated by arrow in Fig. 3d.

3.1.2. Impact toughness

For hot stamping tool steels, impact toughness is a key material property. Fig. 4 shows the effect of post-AM treatments on the Charpy impact toughness and the fracture surfaces obtained after the test. While exhibiting a similar hardness level (about 530 HV_{10}), a relatively low impact energy value of 6.5 J is obtained for the sample with DT treatment (Fig. 4a). Obviously, the QT sample exhibited a significantly better impact toughness of ~17 J, which is 2.6 times of that in DT sample and is comparable to conventional standard H13 steel (15–18 J) [28]. The homogenous microstructure obtained (Fig. 2c and f) after the QT treatment seems to be beneficial to the toughness. In DT samples, the grain/cell size is different at the boundary compared to the center of melt pool. Generally, the zones with fine grain/cell size exhibit greater resistance to deformation. Stress is thus concentrated in the zones with larger grain/cell size, promoting crack initiation there. As shown in Fig. 4b and c, the cleavage facets, characteristic of brittle fracture, were present across most of the fracture surface area in the DT sample.

The shape of the melt pool boundary is depicted by a dashed line in Fig. 4b. It suggests that the melt pool boundaries constitute regions with weaker-bonding in the LB-PBF samples. The weakness of melt pool boundary is also believed to relate to the nonuniform cell structure. Higher cooling rate at the boundaries in the new melt pool side than that in the previous solidified layer made cells finer. Stress concentration on the side with larger cell size promotes crack initiation [29]. Furthermore, the adjacent melt tracks intersect at some points and form angles, where cracks usually initiate [30] and subsequently propagate along these boundaries. Some pores, another source of stress concentration on loading, were found along the melt pool boundaries, as shown in Fig. 4c. In samples subjected to QT treatment, dimples were found, as shown in Fig. 4e. This implies the change in the fracture mechanism from brittle to mixed brittle-ductile one [31]. Compared to DT sample, the microstructure of QT sample is more homogeneous (as shown in Fig. 2c and f), leading to higher impact toughness than that of the DT condition.

3.1.3. Tensile properties

The engineering stress-strain curves are presented in Fig. 5. The corresponding mechanical properties obtained are listed in Table 2. For the DT samples, under the strain rate of 10^{-4} s^{-1}, yield strength ($R_{p0.2}$), tensile strength (R_m) and total elongation (δ) are about 1529 MPa, 1732 MPa and 10.2% respectively. QT treatment leads to a slightly lower strength but marginally better ductility. When the strain rate was increased to 10^{-1} s^{-1}, the strength of the samples under both conditions increased slightly while elongation remained almost unchanged. From the investigation of Åsberg [15], the standard H13 steel manufactured by L-PBF has a yield strength of 1447 MPa after stress relieving followed by standard hardening and tempering treatment, while its elongation at fracture drops to 3.3%. Furthermore, adding an additional hot isostatic pressing step between the above heat treatment, the yield strength increases to 1502 MPa and the elongation at fracture increases to 6.6%. Hence, compared to standard H13 steel fabricated by the same method, M-H13 steel in the present work exhibits acceptable and promising

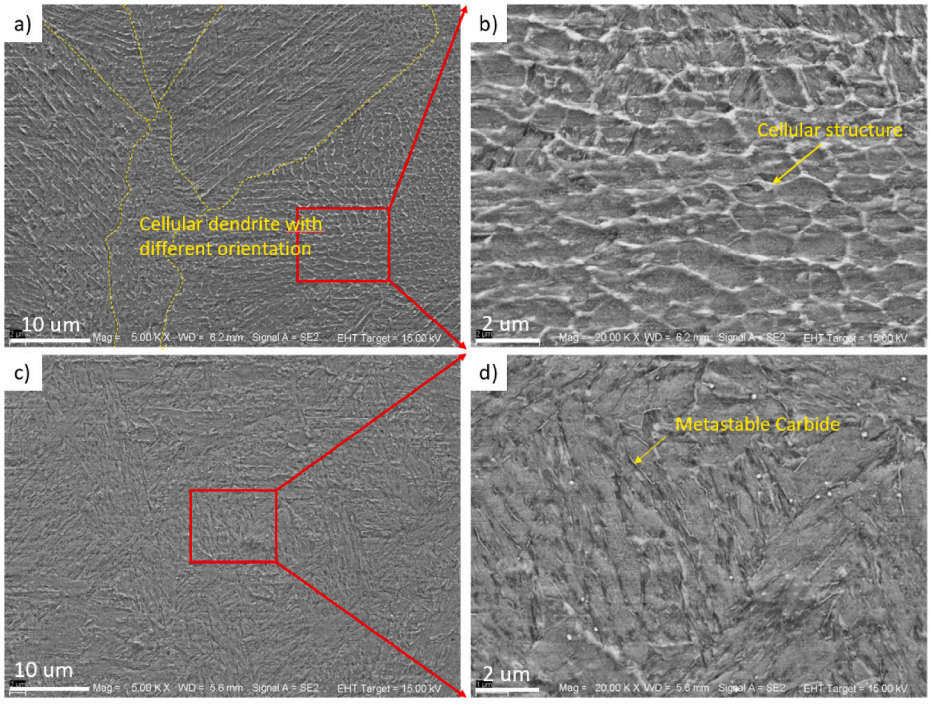

Fig. 3. SEM images showing the microstructure of LB-PBF M-H13 tool steel under different heat treatment: a) and b) for DT; c) and d) for QT.

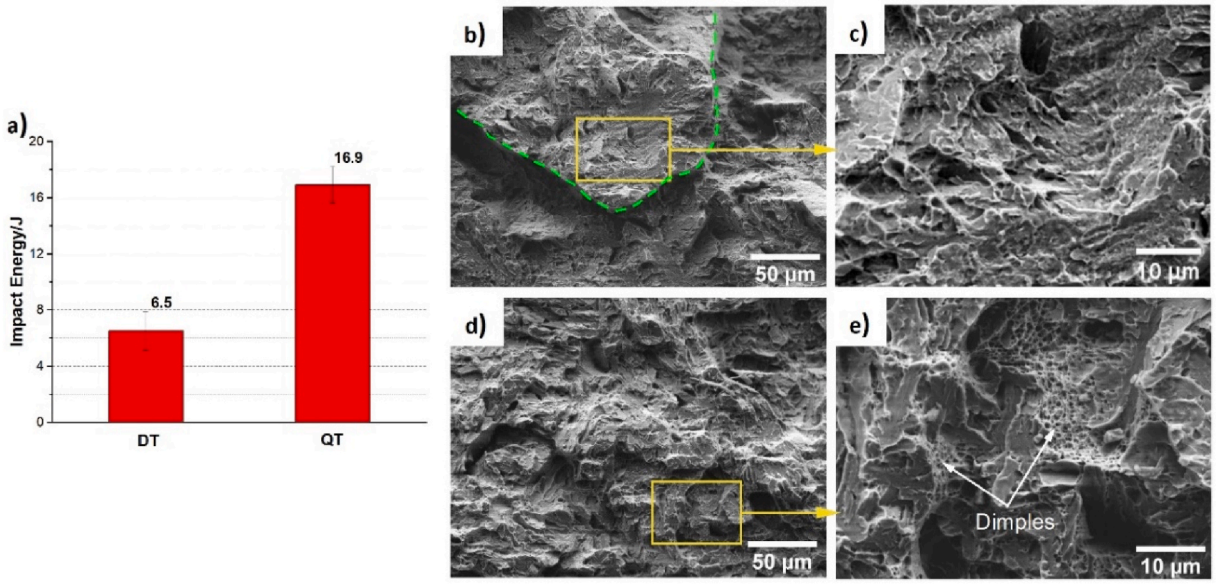

Fig. 4. Impact toughness indicated by absorbed energy (a). SEM images from the fracture surface after Charpy impact test of the samples with DT (b, c) and QT treatment (d, e).

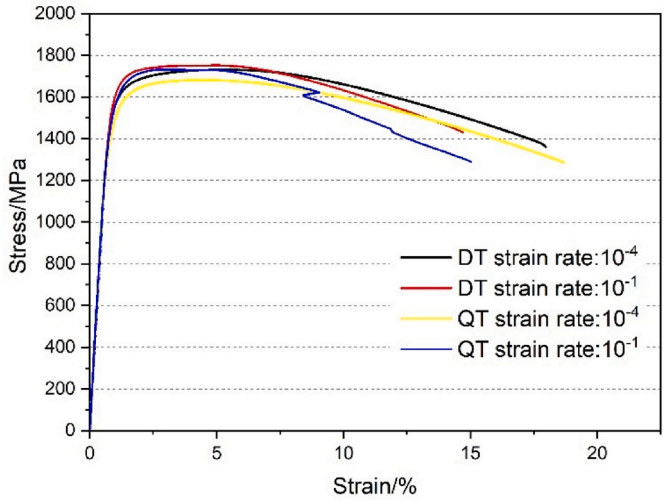

Fig. 5. Engineering stress-strain curves of M-H13 steel under different conditions.

tensile properties.

3.2. Thermal softening resistance

3.2.1. Softening at high temperatures

Hot stamping tools are exposed to work material heat treated at high temperatures. Although the contact time for each part produced is short, a cumulative effect can be expected when subjecting the tool to elevated temperature exposure over a long time during its service. The demands generated on the tool steel used in the dies are hence high. An excellent thermal softening resistance therefore plays a key role in such an application. As an indicator, hardness was measured after a long duration at high temperatures. The evolution of hardness is presented in Fig. 6. After two different post heat treatment (QT and DT) conditions were applied, the samples reached almost the same hardness value of 527 HV_{10}, which is higher than that in as-printed state (501 HV_{10}). The lower hardness from as-printed samples can be attributed to the presence of retained austenite, which was confirmed by XRD-analysis as shown in Fig. 7. Retained austenite is often observed in as-printed condition for LB-PBF tool steels [10,32,33].

Now, considering the evolution of hardness values with heat-treatment time (Fig. 6), the thermal softening resistance is dependent on the post-AM treatment and the conditions of the subsequent exposure at high temperatures. Longer time or higher temperature exposure results in a hardness decrease as expected. Also, the degree of softening was lower at 550 °C isothermal treatment compared to corresponding values at 600 °C. After exposure at 600 °C for 100 h, the hardness decreased dramatically to about 390 HV_{10} for DT sample and 370 HV_{10} for QT samples. For 550 °C, hardness values were still at a moderate level even after longer holding time for both conditions. However, the decrease of hardness is more severe for QT samples. The hardness for the DT sample decreased merely by 8.5% from 527 HV_{10} to 428 HV_{10} after 100 h at 550 °C, while the corresponding decrease for the QT sample was 14.0%. Similar trend was also observed after isothermal holding at 600 °C. For applications where softening resistance determines tool life, DT could be a promising post-AM heat treatment for LB-PBF produced M-H13 tool steel studied.

3.2.2. Microstructure evolution

To further understand the softening response at elevated temperatures, the microstructure evolution was investigated by SEM and XRD. Fig. 7 shows the XRD pattern of the samples under different conditions.

Table 2
The mechanical properties of M-H13 steels under different conditions.

Sample	Strain rate/s^{-1}	$R_{p0.2}$/MPa	R_m/MPa	δ/%	True $R_{p0.2}$/MPa	True R_m/MPa	Strain hardening exponent	Strain rate sensitivity
DT	10^{-4}	1568 ± 9	1736 ± 5	9.9 ± 0.4	1532	1820	0.094	0.00475
DT	10^{-1}	1610 ± 7	1745 ± 9	10.3 ± 0.1	1583	1841	0.081	
QT	10^{-4}	1465 ± 14	1688 ± 9	11.0 ± 0.3	1452	1755	0.111	0.00767
QT	10^{-1}	1514 ± 5	1735 ± 5	10.4 ± 0.6	1529	1776	0.111	

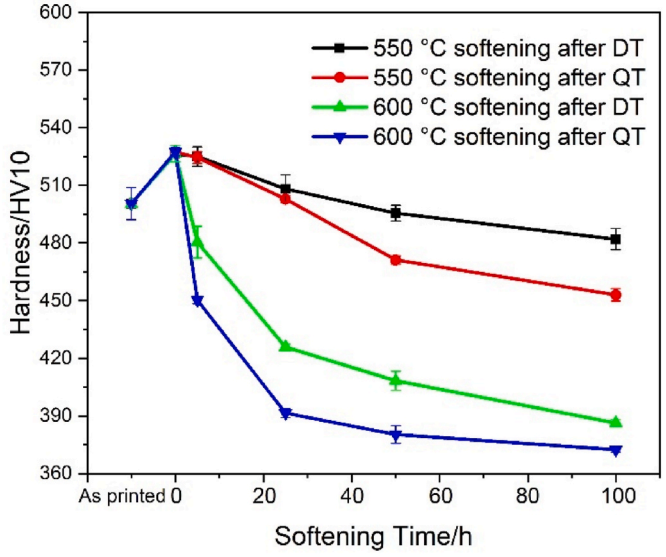

Fig. 6. Hardness of the M-H13 tool steel manufactured by LB-PBF before and after various treatments.

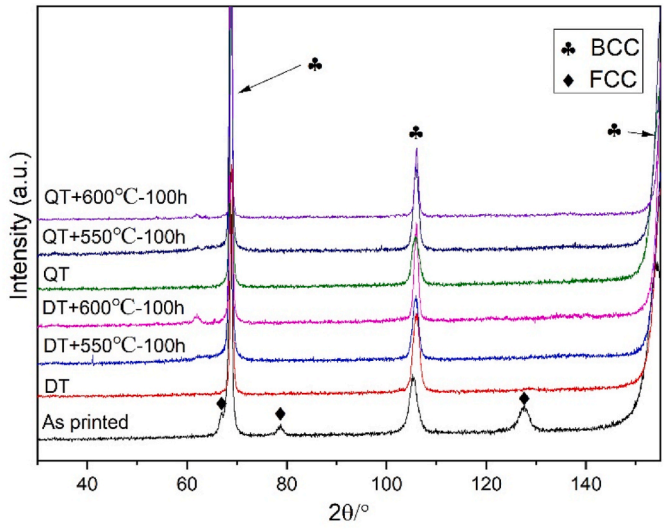

Fig. 7. XRD pattern of the M-H13 tool under various conditions.

In the as-printed condition, bct structure (martensite) was dominant while fcc austenite was also observed. For the samples subjected to post heat treatment and subsequent long-term softening at the chosen temperatures, only bcc ferrite was found, and carbides could not be identified by XRD. Although a small peak emerges in the samples after softening treatment, it is still hard to identify a phase by only one peak. We will try and include this in our future work. Fig. 8 exhibits the microstructure evolution during the thermal softening. For the DT sample, cellular structure can still be seen after treatment at 550 °C for 100h (Fig. 8 a, b). When the temperature was increased to 600 °C, the cellular structure disappeared and was replaced by a microstructure that contains a large number of finely dispersed particles and some coarse particles (Fig. 8 c, d). When the QT samples were subjected to 550 °C-100 h treatment, the rod-shaped carbides in the QT state (Fig. 3d) were dissolved in the matrix and fine carbides instead appear. The whitish round particles still exist as before (Fig. 8 e, f), which indicates these round particles are relatively thermal stable. With the increase of temperature to 600 °C, the fraction of tiny carbides also increased substantially; meanwhile, the white round carbides coarsened, as seen in Fig. 8 g, h. The evolution and identification of carbides will be further discussed in Part 4.2.

4. Discussions

4.1. Relationship between mechanical properties and microstructure in steel with two post processing routes

As shown in Table 2, the difference in tensile properties of both DT and QT samples are rather small. Still, the strengthening mechanisms behind their behavior are different to certain extent. For the DT sample, the strength is supposed to be attributed to both tempered martensite and fine cellular microstructure. Although the preheating temperature of base plate is 200 °C, martensite phase would still be formed during the LB-PBF process. Based on JmatPro simulation, the temperature corresponding to martensite start (M_s) and 90% transformation are 283 °C and 160 °C respectively. This means the steel will transform after printing and subsequently cooling to the room temperature. It is to be noticed that upon DT treatment, the martensite will transform into tempered martensite and contribute to its high strength. Regarding the cellular structure, their boundaries are supposed to consist of micro-segregation and dislocation entanglement. Similar to grain boundaries, these boundaries may hinder the movement of dislocations and improve the mechanical properties of materials. For the QT sample, the strengthening originates from a complex microstructure of tempered martensite with uniformly dispersed fine carbides along the lath boundaries (Fig. 3d). After austenitization, martensite is formed by quenching. During tempering, the material will transform to tempered martensite. Meanwhile, carbides nucleate homogeneously from austenite, providing precipitation strengthening effect [34]. These carbides are likely M_7C_3 and M_3C type from the simulation in Fig. 9.

It has been found that when the strain rate was increased from 10^{-4} s^{-1} to 10^{-1} s^{-1}, the strength of both DT and QT samples increased. The strain rate sensitivity (*SRS*) can be calculated using the power-law relationship($\sigma = \alpha\dot{\varepsilon}^m$) [35], where σ is the stress, α a material related constant, m strain rate sensitivity and $\dot{\varepsilon}$ strain rate. For true stress σ_y at yielding (Table 2), the formula describing power-law dependence and strain rate sensitivity are given in Eqs. (1) and (2).

$$(\sigma_y)_{DT} = 1644\dot{\varepsilon}^{0.00475}, \cdot\mathrm{SRS}\cdot = \cdot 0.00475 \quad (1)$$

$$(\sigma_y)_{QT} = 1597\dot{\varepsilon}^{0.00767}, \cdot\mathrm{SRS}\cdot = \cdot 0.00767 \quad (2)$$

From the above analysis, it can be concluded that the QT condition has higher SRS value than the DT condition. According to Hart's instability criterion [36], nonuniform deformation starts if the condition in Eq. (3) is met

$$\frac{1}{\sigma}\left(\frac{\partial\sigma}{\partial\varepsilon}\right)_{\dot{\varepsilon}} - 1 + m \leq 0 \quad (3)$$

Where σ and ε represent true stress and true strain respectively. Obviously, higher strain rate sensitivity (m) means delayed localized deformation (necking) and consequently better ductility. This explains partly why QT sample with a higher m value exhibits a larger total elongation compared to DT sample when subjected to tensile stress under different strain rates investigated. For bcc metal materials, SRS depends on the mean grain size d [37,38], and is usually in the order of 0.04–0.004. Wang [37] found that m decreased dramatically with grain size. However, when the d value is extremely small (≤~20 nm), this tendency could reverse [39]. In this study, the M-H13 steel has fine microstructure in as-printed condition owing to the fast-cooling rate, whereby the DT condition having a direct memory of the as-printed microstructure also has a low m value.

Another important factor that determines the start of nonuniform necking in Eq. (3) is strain hardening rate $\frac{\partial\sigma}{\partial\varepsilon}$. Hollomon's equation $\sigma = K\varepsilon^n$ is often used to describe the relationship between true stress σ and

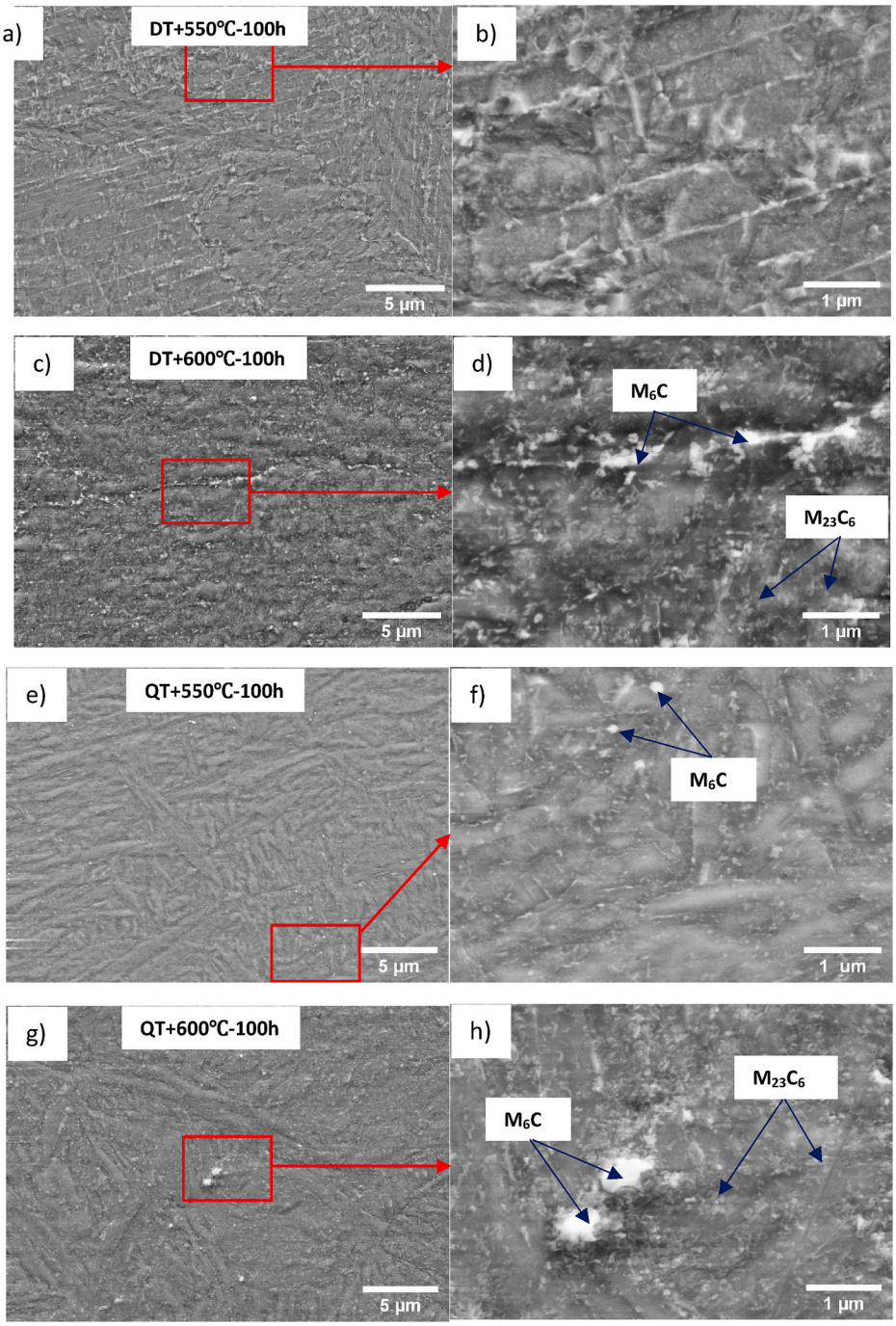

Fig. 8. SEM images of the M-H13 tool steel after the test of thermal softening resistance: a, b) DT+550°C-100h; c, d) DT+600 °C- 100 h; e, f) QT+550 °C- 100 h; g, h) QT+600 °C- 100 h.

true train ε, where K is a constant and n is strain hardening exponent. Apparently, $\frac{\partial\sigma}{\partial\varepsilon}$ is closely correlated to the strain hardening exponent n. Larger n means higher strain hardening rate $\frac{\partial\sigma}{\partial\varepsilon}$. In the present work, fitting tensile curves using Hollomon's equation gives the n value under different conditions, as shown in Table 2. DT sample had n values of 0.094 and 0.081 at strain rate of 10^{-4} and 10^{-1}, respectively. The n value of QT sample at both strain rates is 0.111, which is higher than that of DT sample. Higher strain hardening exponent will contribute to an improved ductility.

As discussed previously, different microstructures are obtained after different post treatment conditions examined. Compared with DT sample, melt pool boundaries, which are weak-bonding regions with potential defects, disappear in QT sample, leading to a more homogeneous composition and microstructure. In addition, cellular structure with micro-segregation and dislocation entanglement is removed. QT state is also able to provide more uniformly distributed carbides. It is hypothesized that it is this modification of microstructure that gives rise to higher work hardening ability and larger strain rate sensitivity.

As shown in Fig. 4, impact toughness of the QT samples is nearly 3 times compared to the DT samples. Impact test is a dynamic test with extremely high strain rate. Impact toughness essentially is the energy absorbed by material before fracture, which is determined by both strength and ductility. Compared to the DT sample, strain rate sensitivity and strain hardening exponent for the QT sample increases by 61% and 27% respectively. Higher strain rate sensitivity means stronger effect of

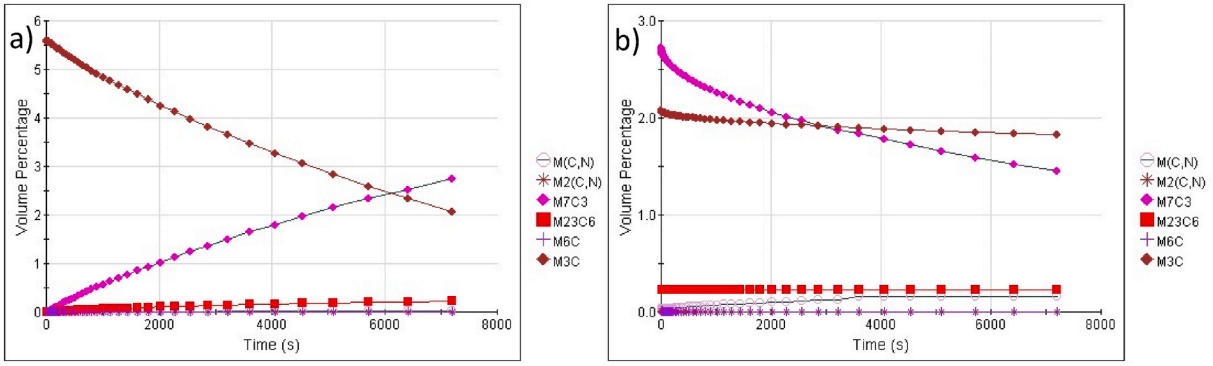

Fig. 9. Precipitation behavior simulated by JMatPro in M-H13 steel after solution treatment at 1020 °C and tempered in two stages of 580 °C for 2 × 2 h (a) the 1st stage (b) the 2nd stage.

strain rate hardening, leading to significantly enhanced strength at high strain rate. Also, larger work hardening capability of the QT sample delays necking, leading to increased ductility. Hence, the significant impact toughness of the QT samples is the combined result of the higher strain rate sensitivity and higher work hardening when compared with the DT sample.

4.2. Carbide identification

As shown in Fig. 3, rod-shape precipitates were detected in QT samples. Fig. 9 shows the simulated volume fraction of precipitates after solution treatment at 1020 °C followed by two stage tempering at 580 °C for 2 × 2 h. During the first stage tempering (Fig. 9a), M_3C carbide forms first followed by M_7C_3. The volume fraction of M_3C decreases gradually with time. At the subsequent stage of tempering, $M_{23}C_6$ starts to form. During the second stage of tempering (Fig. 9b), the volume fraction of both M_7C_3 and M_3C decreases with time, implying these two phases are metastable and will dissolve with long-time exposure. At the later stage of tempering, M(C,N) starts to form. Anyhow, the dominant carbides are M_7C_3 and M_3C. From the simulation results, the carbide size (not shown here) of M_3C is between 130 and 140 nm, while the carbide size of M_7C_3 is smaller than 40 nm. This means that the rod carbides in Fig. 3d might be M_3C. Under the equilibrium state at 550 °C or 600 °C, the M_7C_3 and M_3C carbides do not exist, as shown by JMatPro simulation in Fig. 10. Microstructural observation of QT sample after softening treatment of 550 °C for 100 h indicated that the carbides in rod-shape (M_3C) decreased extensively, as exhibited in Fig. 8f. This is consistent with the simulation results.

It is well known that elevated temperature and long duration heat treatments may lead to a state close to thermal equilibrium. To identify the carbides formed during long term treatment at high temperature along with their fraction as well as composition, simulation using JMatPro software was performed at the equilibrium condition. As shown in Fig. 10, M(C, N) carbide starts to precipitate at 1250 °C with a volume fraction of 0.56% at temperatures below ~ 1000 °C. M_6C carbide precipitates from austenite phase at 1011 °C with a volume fraction about 2% when temperature is below 744 °C. $M_{23}C_6$ carbide with a fraction of 5% is formed during the later stage of cooling. Table 3 lists the major elements in the carbides and their concentration calculated with JMatPro. It can be seen that M(C,N) carbonitride should be V(C,N). M_6C and $M_{23}C_6$ carbides are supposed to be $(Mo, Fe, W)_6C$ and $(Cr, Fe, Mo)_{23}C_6$, respectively. Based on the simulation results obtained, a preliminary assumption could be made that the bright round particles observed in Figs. 3 and 8 could be M_6C carbide owing to the low volume fraction. Notice the start temperature of precipitation (1011 °C) of the M_6C is close to the austenitization temperature (1020 °C). A small amount of M_6C carbides (the whitish round particles) in QT sample (Fig. 3d) can be expected. Considering that the fine particles develop gradually, they are likely $M_{23}C_6$ carbide. In fact, the microstructure in Fig. 8d and h is similar. This is expected because both DT and QT samples have been subjected to long time treatment (100 h) at relatively high temperature of 600 °C.

EDS analysis was performed on the carbides on a QT sample annealed at 550 °C for 100 h (Fig. 11a). The Fe, Cr, Mo, V, W and C elemental maps are shown in Fig. 11b. The round particles with a size of 150 nm are enriched with C, Mo, and W, indicating M_6C carbides (Table 3). M_6C particles with a size of 120 nm is also revealed in a TEM dark field image in the DT sample annealed at 600 °C for 100 h

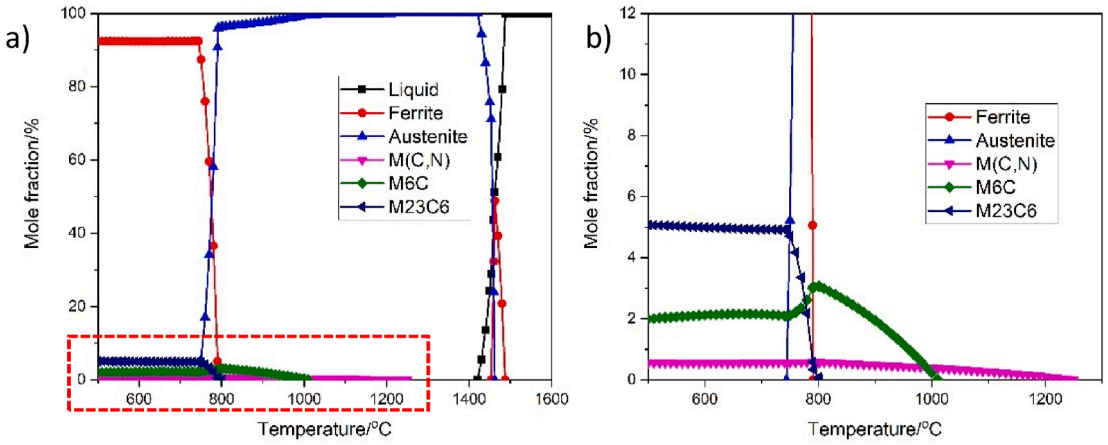

Fig. 10. JMatPro simulation of mole fraction of phases vs temperature for M-H13 steel, a) complete simulation diagram, and b) regional zoom in diagram to reveal carbides formation in equilibrium condition.

Table 3
Concentration of major elements (at%) in carbides calculated by JMatPro.

Temperature/°C	Phase	C	N	Cr	Mo	V	W	Fe
550	M(C,N)	18.77	28.87	1.45	0.02	50.86	0	0.03
	M_6C	14.29	0	4.99	29.98	0.36	14.32	34.60
	$M_{23}C_6$	20.69	0	42.66	9.45	0.47	0.13	23.63
600	M(C,N)	18.85	29.01	2.26	0.04	49.79	0	0.05
	M_6C	14.29	0	5.42	28.69	0.45	13.48	36.14
	$M_{23}C_6$	20.69	0	39.47	9.00	0.51	0.18	27.56

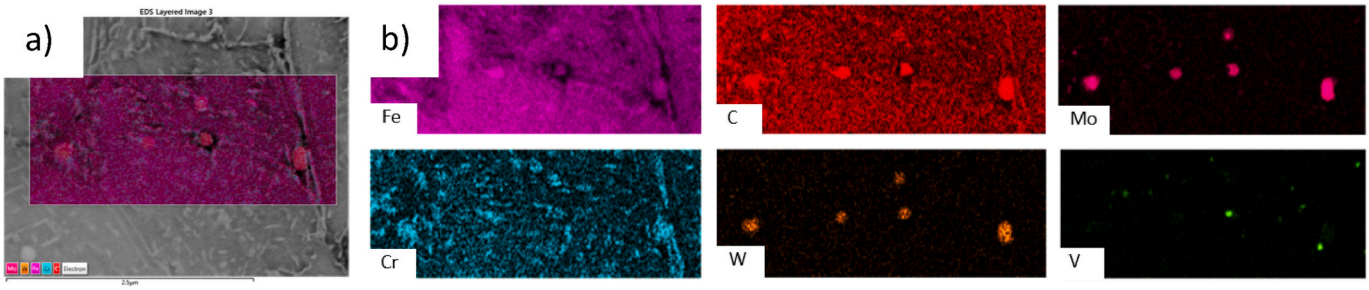

Fig. 11. a) SEM image and b) EDS mapping of different carbides in QT+550°C-100h sample.

(Fig. 12a). It is identified by a SAED pattern oriented close to the $[\bar{2}23]_{M6C}$ zone axis (Fig. 12b). High V-containing particles with a size of 50 nm are often observed neighboring the M_6C particles, and the Cr-enriched fine particles are dispersed in the matrix. The observed V-enriched and Cr-enriched particles could be the V(C,N) and $M_{23}C_6$ types of carbides, as estimated by the JMatPro simulation in Fig. 10 and Table 3.

4.3. Thermal softening resistance

As shown in Fig. 6, the hardness of the material is almost identical after two different post heat treatments (QT and DT). After being further treated at 550 °C for 100 h, the hardness drops 8.5% and 14.0% for DT and QT sample. The corresponding hardness reduction at 600 °C was 26.8% and 29.4%, respectively. It indicates that DT sample still has a better softening resistance than QT. This can be explained as follows.

As discussed in section 4.2, the strengthening mechanisms differ from the microstructure point of view. The high hardness in DT sample is attributed to tempered martensite and the fine cellular structure. In the QT sample, it is supposed to be related to tempered martensite and the metastable M_7C_3 and M_3C carbides along the lath boundaries. After isothermal treatment at 550 °C for 100 h, cellular structure still exists in DT sample. However, the metastable carbides in QT samples are dissolved into the matrix and hardening effect is therefore lost to some extent. While the influence from dislocation evolution isn't significant at 550 °C due the insufficient kinetic condition [40]. As a result, DT samples have a better thermal softening resistance than QT samples.

Secondary V(C, N) might be also beneficial to the better softening resistance of DT. In QT sample, most of the V(C, N) is formed during the austenitization (refer to Fig. 10b), which provide less effective hardening. Only relative low fraction of secondary V(C, N) will be available during long-term softening treatment. In DT sample, on the other hand, little V(C, N) was formed at beginning. V(C, N) particles could be precipitated during tempering. Generally, the M(C, N) particle has a higher resistance to coarsening than Cr-enriched $M_{23}C_6$ carbides [40]. As we can see, these V(C, N) particles remains a small size during the long-term softening treatment (Fig. 11b), which indicates that they are stable and could contribute to improved softening resistance during the long-term treatment. Detailed investigation of how evolution of carbides affects the softening behavior is of interest.

Smaller grain size of ferrite is another important reason for better softening resistance in DT samples. This can also be depicted from the

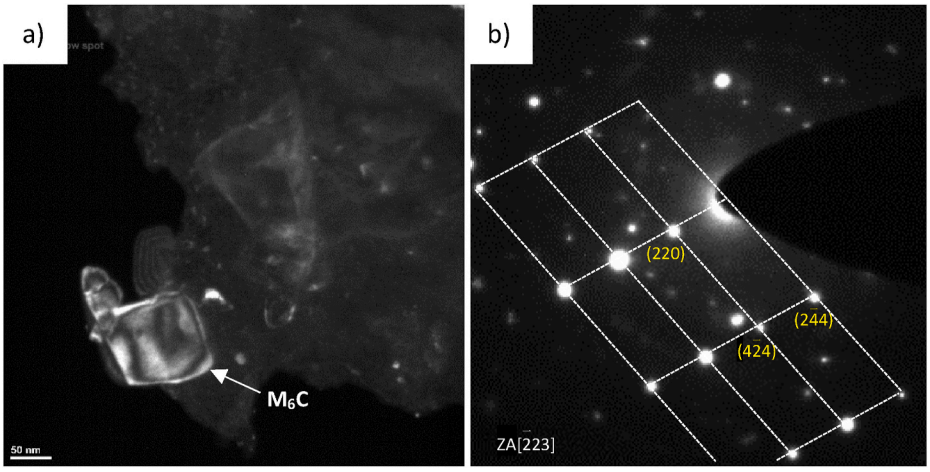

Fig. 12. TEM micrograph of DT + 600 °C-100 h sample; a) dark field image; b) the selected area electron diffraction pattern with the $[\bar{2}23]$ zone axis of the particle in the image.

XRD patterns. The full width at half maxima (FWHM) of bcc diffraction lines from XRD pattern in Fig. 7 can reflect the microstructural evolution. As shown in Table 4, for {110} peak, the DT samples show larger FWHM values (0.607, and 0.423) than those of the QT samples (0.558, and 0.413) at both softening temperatures of 550 °C and 600 °C. This means the DT samples have a finer grain size, leading to higher hardness and consequently a better thermal softening resistance than the QT sample.

As revealed by Fig. 6, the hardness of M-H13 steel deteriorated dramatically at 600 °C. As shown in Fig. 6, the hardness drops rapidly at the initial 600 °C holding for both DT sample and QT sample even difference previous tempering temperatures have been adopted (625 °C for QT, 585 °C for DT). The decrease in hardness and initial softening at 600 °C was greatly attributed from the rapid dislocation decrease [40]. Regardless the different level of dislocation density they have before, the density would tend to stable after a 25 h holding. The rapid hardness drop is also related to the grain growth of ferrite, at least partly. As shown in Table 4, the FWHM values of both {110} and {200} peaks are decreased with the temperature increasing from 550 °C to 600 °C in both DT and QT samples. The FWHM value may be related to the grain size, dislocation density and residual stresses. However, the vast majority of residual stresses should be relieved in the DT and QT samples. Moreover, in some perspective, the grain boundaries can be considered as an assembly of dislocations. Therefore, the decrease of FWHM value could be considered as the coarsening of ferrite structure.

Table 4
Line position and FWHM of (110) and (200) bcc from XRD patterns.

Sample	2-Theta of {110} Peak/°	FWHM	2-Theta of {200} Peak/°	FWHM
As-Printed	68.659	0.837	105.396	2.143
DT	68.918	0.631	105.986	1.626
DT+550 °C- 100 h	68.724	0.607	105.848	1.497
DT+600 °C- 100 h	68.856	0.423	105.972	1.051
QT	68.794	0.682	105.843	1.783
QT+550 °C- 100 h	68.765	0.558	105.936	1.306
QT+600 °C- 100 h	68.814	0.413	105.990	0.976

5. Conclusion

In this study, a modified H13 tool steel was printed successfully by means of laser beam powder bed fusion (LB-PBF). Two different post-AM heat treatment routes, i.e., direct tempering (DT) and conventional quenching followed by two stage tempering (QT), were applied and the effect on mechanical properties and microstructure was examined. In addition, softening resistance and related microstructural evolution at elevated temperature of 550 and 600 °C were investigated. The purpose was to arrive at structure-property relationship for the material studied after printing. The main conclusions obtained from this study can be presented as follows.

1. In the as-printed material, distinct melt pool boundaries and cellular structure were observed. After direct tempering (DT), the boundaries still remained but were less clear and the cellular structure in the size range of ~1 μm was maintained. The QT process results in the melt pool boundaries and cellular structure to disappear, leading to a more homogeneous microstructure of lath tempered martensite.
2. The samples in DT and QT condition had almost the same hardness value of 527 HV_{10}, which is higher than that of the as-printed sample. The material heat-treated by both routes exhibit comparable tensile properties to conventional H13 steel. The yield and tensile strength values reached levels of 1500 MPa and 1700 MPa combined with 10% elongation. Specifically, QT treatment leads to a slightly lower tensile strength but marginally better ductility. When the strain rate was increased from 10^{-4} s^{-1} to 10^{-1} s^{-1}, the strength of the samples under both conditions increased slightly while elongation remained almost unchanged.
3. Charpy impact test was employed to depict the impact toughness. The results showed that QT samples had a considerable higher impact toughness than DT sample. This was attributed to the higher strain rate sensitivity and higher work hardening ability originating from different microstructure.
4. Thermal softening resistance is dependent on the post-AM treatment and the conditions of subsequent exposure at high temperatures. Longer time or higher temperature exposure results in a decrease in hardness. Lower degree of softening was observed for 550 °C than that for 600 °C holding. The decrease in hardness is more severe for QT samples. It is supposed that smaller grain size of ferrite, less coarsened carbides and the cellular structure being preserved contribute to DT samples exhibiting higher softening resistance.
5. During the softening test, the evolution of carbides in the steels was analyzed by combined experimental and numerical methods. In QT process, the rod-shaped carbides can be M_3C. The M_3C carbides dissolve into the matrix when subjected to further heat treatment, and fine $M_{23}C_6$ and M(C,N) would be formed. With the increase in temperature to 600 °C, carbides may become coarsened. In all conditions, M_6C was identified. For DT sample, the cellular structure still remained after treatment at 550 °C for 100h. When the temperature was increased to 600 °C, the cellular structure disappeared and was replaced by a structure containing densely dispersed carbides.

CRediT authorship contribution statement

Miwen Yuan: Investigation, Data curation, Writing – original draft. **Yu Cao:** Writing – review & editing, Supervision. **Seshendra Karamchedu:** Conceptualization, Methodology, Writing – review & editing. **Seyed Hosseini:** Resources, Methodology. **Yiming Yao:** Investigation. **Johan Berglund:** Resources, Methodology. **Libin Liu:** Software, Supervision. **Lars Nyborg:** Supervision.

Declaration of competing interest

The authors declare that they have no known competing financial interests or personal relationships that could have appeared to influence the work reported in this paper.

Acknowledgements

This study is supported by Vinnova (Sweden's Innovation Agency) No. 2016–03305, China Scholarship Council (CSC) and Production Area of Advance, Chalmers University of Technology, Sweden.

References

[1] M.S. Shinde, K.M. Ashtankar, Additive manufacturing-assisted conformal cooling channels in mold manufacturing processes, Adv. Mech. Eng. 9 (2017) 1–14.
[2] D. Zhang, et al., Metal alloys for fusion-based additive manufacturing, Adv. Eng. Mater. 20 (2018) 1–20.
[3] M. Elsayed, M. Ghazy, Y. Youssef, K. Essa, Optimization of SLM process parameters for Ti6Al4V medical implants, Rapid Prototyp. J. 25 (2019) 433–447.
[4] N.T. Aboulkhair, I. Maskery, C. Tuck, et al., The microstructure and mechanical properties of selectively laser melted AlSi10Mg: the effect of a conventional T6-like heat treatment, Mater. Sci. Eng., A 667 (2016) 139–146.
[5] V.A. Popovich, E.V. Borisov, A.A. Popovich, et al., Functionally graded Inconel 718 processed by additive manufacturing: crystallographic texture, anisotropy of microstructure and mechanical properties, Mater. Des. 114 (2017) 441–449.
[6] R. Casati, M. Coduri, N. Lecis, C. Andrianopoli, M. Vedani, Microstructure and mechanical behavior of hot-work tool steels processed by Selective Laser Melting, Mater. Char. 137 (2018) 50–57.
[7] D. Herzog, V. Seyda, E. Wycisk, C. Emmelmann, Additive manufacturing of metals, Acta Mater. 117 (2016) 371–392.
[8] D.D. Gu, Y.C. Hagedorn, W. Meiners, G.B. Meng, R.J.S. Batista, K. Wissenbach, R. Poprawe, Densification behavior, microstructure evolution, and wear

performance of selective laser melting processed commercially pure titanium, Acta Mater. 60 (2012) 3849–3860.
[9] M. Lin, X. Zhao, L. Han, Q. Liu, J. Gu, Microstructural evolution and carbide precipitation in a heat-treated H13 hot work mold steel, Metallogr. Microstruct. Anal. 5 (2016) 520–527.
[10] R. Mertens, B. Vrancken, N. Holmstock, Y. Kinds, J.P. Kruth, J. Van Humbeeck, Influence of powder bed preheating on microstructure and mechanical properties of H13 tool steel SLM parts, Phys. Procedia. 83 (2016) 882–890.
[11] L. Wang, J. Wu, X. Huang, X. Hong, SLM-manufactured 30CrMnSiA alloy: mechanical properties and microstructural effects of designed heat treatment, Opt Laser. Technol. 107 (2018) 89–98.
[12] J. Lee, et al., Microstructural effects on the tensile and fracture behavior of selective laser melted H13 tool steel under varying conditions, Mater. Char. 155 (2019) 109817.
[13] M.J. Holzweissig, A. Taube, F. Brenne, M. Schaper, T. Niendorf, Microstructural characterization and mechanical performance of hot work tool steel processed by selective laser melting, Metall. Mater. Trans. B Process Metall. Mater. Process. Sci. 46 (2015) 545–549.
[14] T.V. Philip, T.J. McCaffrey, Ultrahigh strength steels, in: G.T. Murray (Ed.), Handb. Mater. Sel. Eng. Appl, CRC Press, New York, 1997, pp. 149–162.
[15] M. Åsberg, G. Fredriksson, S. Hatami, W. Fredriksson, P. Krakhmalev, In fl uence of post treatment on microstructure , porosity and mechanical properties of additive manufactured H13 tool steel, Mater. Sci. Eng., A 742 (2019) 584–589.
[16] S.A. Khairallah, A.T. Anderson, A. Rubenchik, W.E. King, Laser powder-bed fusion additive manufacturing: physics of complex melt flow and formation mechanisms of pores, spatter, and denudation zones, Acta Mater. 108 (2016) 36–45.
[17] D. Dqg, V. Ri, S. Iru, K. Ghqvlw, W.V. Sduwv, Optimization and simulation of SLM process for high density H13 tool steel parts, Phys. Procedia. 83 (2016) 26–35.
[18] D. Wang, Y. Yang, Z. Yi, X. Su, Research on the fabricating quality optimization of the overhanging surface in SLM process, Int. J. Adv. Manuf. Technol. 65 (2013) 1471–1484.
[19] S. Giganto, P. Zapico, M.Á. Castro-Sastre, S. Martínez-Pellitero, P. Leo, P. Perulli, Influence of the scanning strategy parameters upon the quality of the SLM parts, Procedia Manuf 41 (2019) 698–705.
[20] T.M. Mower, M.J. Long, Mechanical behavior of additive manufactured, powder-bed laser-fused materials, Mater. Sci. Eng., A 651 (2016) 198–213.
[21] W. Do Yoo, J.H. Lee, K.T. Youn, Y.M. Rhyim, Study on the microstructure and mechanical properties of 17-4 PH stainless steel depending on heat treatment and aging time, Solid State Phenom. 118 (2006) 15–20.
[22] H. Chen, D. Gu, D. Dai, C. Ma, M. Xia, Microstructure and composition homogeneity , tensile property , and underlying thermal physical mechanism of selective laser melting tool steel parts, Mater. Sci. Eng., A 682 (2017) 279–289.
[23] S.B. Anders Kvarned1, Oikonomou1 Christos, et al., Uddeholm AM, Heatvar R : a new AM material with excellent high-temperature properties for demanding Hot Work applications, Int. J. Met. 2 (2019) 47–55.
[24] F. Deirmina, N. Peghini, B. Almangour, D. Grzesiak, M. Pellizzari, Heat treatment and properties of a hot work tool steel fabricated by additive manufacturing, Mater. Sci. Eng., A 753 (2019) 109–121.
[25] D. Kono, A. Maruhashi, I. Yamaji, Y. Oda, M. Mori, Effects of cladding path on workpiece geometry and impact toughness in Directed Energy Deposition of 316L stainless steel, CIRP Annals 67 (2018) 233–236.
[26] J. Sander, J. Hufenbach, L. Giebeler, M. Bleckmann, J. Eckert, U. Kühn, Microstructure, mechanical behavior, and wear properties of FeCrMoVC steel prepared by selective laser melting and casting, Scripta Mater. 126 (2017) 41–44.
[27] J. Krell, A. Röttger, K. Geenen, W. Theisen, General investigations on processing tool steel X40CrMoV5-1 with selective laser melting, J. Mater. Process. Technol. 255 (2018) 679–688.
[28] M. Koneshlou, K. Meshinchi Asl, F. Khomamizadeh, Effect of cryogenic treatment on microstructure, mechanical and wear behaviors of AISI H13 hot work tool steel, Cryogenics 51 (2011) 55–61, 2011.
[29] Z.H. Xiong, S.L. Liu, S.F. Li, Y. Shi, Y.F. Yang, R.D.K. Misra, Role of melt pool boundary condition in determining the mechanical properties of selective laser melting AlSi10Mg alloy, Mater. Sci. Eng., A 740–741 (2019) 148–156.
[30] W. Shifeng, L. Shuai, W. Qingsong, C. Yan, Z. Sheng, S. Yusheng, Effect of molten pool boundaries on the mechanical properties of selective laser melting parts, J. Mater. Process. Technol. 214 (2014) 2660–2667.
[31] L. zhi Wang, J. jiao Wu, X. fei Huang, X. fu Hong, SLM-manufactured 30CrMnSiA alloy: mechanical properties and microstructural effects of designed heat treatment, Opt Laser. Technol. 107 (2018) 89–98.
[32] G. Telasang, J. Dutta Majumdar, I. Manna, G. Padmanabham, M. Tak, Effect of laser parameters on microstructure and hardness of laser clad and tempered AISI H13 tool steel, Surf. Coating. Technol. 258 (2014) 1108–1118.
[33] K.M. McHugh, Y. Lin, Y. Zhou, E.J. Lavernia, Influence of cooling rate on phase formation in spray-formed H13 tool steel, Mater. Sci. Eng., A 477 (2008) 50–57.
[34] P. Kürnsteiner, M.B. Wilms, A. Weisheit, P. Barriobero-Vila, E.A. Jägle, D. Raabe, Massive nanoprecipitation in an Fe-19Ni-xAl maraging steel triggered by the intrinsic heat treatment during laser metal deposition, Acta Mater. 129 (2017) 52–60.
[35] N.V. Nguyen, T.H. Pham, S.E. Kim, Microstructure and strain rate sensitivity behavior of SM490 structural steel weld zone investigated using indentation, Construct. Build. Mater. 206 (2019) 410–418.
[36] E.W. Hart, Theory of the tensile test, Acta Metall. 15 (1967) 351–355.
[37] Y.M. Wang, E. Ma, Strain hardening, strain rate sensitivity, and ductility of nanostructured metals, Mater. Sci. Eng., A 375–377 (2004) 46–52.
[38] T.R. Malow, C.C. Koch, P.Q. Miraglia, K.L. Murty, Compressive mechanical behavior of nanocrystalline Fe investigated with an automated ball indentation technique, Mater. Sci. Eng., A 252 (1998) 36–43.
[39] D. Jang, M. Atzmon, Grain-size dependence of plastic deformation in nanocrystalline Fe, J. Appl. Phys. 93 (2003) 9282–9286.
[40] J. Sjöström, Chromium Martensitic Hot-Work Tool Steels, PhD Diss, 2004.